Digital laser for on-demand intracavity selective excitation of second harmonic higher-order modes

Teboho Bell,[1,2,*] **Mosima Kgomo,**[1] **and Sandile Ngcobo**[1]

[1] *Council for Scientific and Industrial Research, Meiring Naude Rd, Pretoria, South Africa*
[2] *University of KwaZulu-Natal, University Road, Durban, South Africa*
*tbell@csir.co.za

Abstract: In this article, we demonstrate selective excitation of second harmonic higher-order modes inside a diode end-pumped solid-state laser resonator that comprises of a nonlinear potassium titanyl phosphate (KTP) crystal and a digitally addressed holographic end-mirror in a form of a reflective phase-only spatial light modulator (SLM). The emitted second harmonic higher-order modes at 532 nm are generated by an intracavity nonlinear KTP crystal that is pumped by high-order fundamental modes operating at 1064 nm. The fundamental modes are digitally controlled by displaying a computer-generated hologram in the form of a grey-scale image to the SLM screen for on-demand high-order modes. The phase matching of the fundamental mode to the generated frequency-doubled mode is achieved by controlling the phase of the digital hologram to either achieve a high or quasi-degree of orbital angular momentum conservation. We show that we can intracavity generate frequency-doubled high-order Laguerre-Gaussian modes and Hermit-Gaussian modes that are either quasi or fully reproducible in the far-field. To the best of our knowledge, this is the first laser to generate frequency-doubled on-demand higher-order modes inside the cavity at the visible (green) wavelength of 532 nm.

1. Introduction

Green laser beams generated using frequency doubling or wave mixing which is a nonlinear process also known as second harmonic generation (SHG) technique have been extensively used in laser detection [1], spectroscopy [2], laser ranging [3], ocean exploitation [4], medical surgeries [5], particle manipulation [6], quantum communication [7], and military applications [8]. The general scheme that has been prevalent for nonlinear wave mixing has normally involved using laser beams with a Gaussian TEM_{00} profile since they are emitted by most laser resonators. The generated green laser beam from either inside [9,10] or outside [11] the laser cavity will then be customised and shaped using additional optical elements such as apertures, lenses and diffractive optical elements to the desired beam profile. In this paper, we will demonstrate a novel method that shows it is now possible to realise on-demand spatial shaping of frequency-doubled laser modes within a laser cavity. The motivation for developing this novel method has been to save cost and develop a compact system such that the normal approach of initial frequency doubling the beam and then later manipulate the spatial profile of the beam will be seen to be not worthwhile and cumbersome.

The nonlinear crystal that was utilised to exploit its birefringence to generate second harmonic high order modes is Potassium Titanyl Phosphate (KTP) crystal [12,13]. The nonlinear KTP crystal was chosen since it has a relatively high SHG coefficient, high damage threshold, great optical nonlinearity and an excellent thermal stability [14,15]. It should be stated that much other nonlinear crystals can be incorporated into the Green Digital Laser for frequency doubling or wave mixing of high-order modes, such nonlinear crystals are *BBO* (β-barium borate), *KDP* (potassium dihydrogen phosphate), $LiNbO_3$ (lithium niobate), and LiB_3O_5 (lithium triborate) [16,17]. These

nonlinear crystals have the appropriate optical properties such as strong birefringent, crystal symmetry, high damage threshold and good transparency for both the fundamental pump beam and the frequency-doubled or mixed beam [18–20].

In this article, we made use of our newly developed diode-end-pumped Nd: YAG solid-state Digital Laser that operates at 1064 nm [21–25], to create the fundamental frequency for pumping the intracavity nonlinear crystal so as to generate second harmonic frequency at 532 nm and make the Digital Laser emits green laser beam, Green Digital Laser. The utilisation of the diode laser as a source of energy for the Green Digital Laser provided an advantage of having a source with a stable frequency, high brightness, long lifetime and better efficiency, especially when an end-pump setup is used such that the pump mode and the fundamental mode are matched. The second advantage of using the Green Digital Laser is its ability to generate and switching between spatial high-order modes in real-time just by displaying a grey-scale digital hologram image on the screen of the Spatial Light Modulator (SLM) that has been integrated as the end-mirror of the resonator. The incorporation of the SLM in the Green Digital Laser cavity creates an advantage of allowing extensive dynamic range of phase holograms to be introduced on the fundamental mode inside the laser cavity such that the phase-matching inside the non-linear crystal of the fundamental mode and the generated second harmonic mode produces a wide range of spatial profiles that can either be out-of-phase, quasi-phase [9,26] or purely in-phase [11,27]. In this article we show for the very first time that we can in real-time, intracavity generate both quasi-phase and purely in-phase frequency-doubled high-order Laguerre-Gaussian Modes and Hermit-Gaussian modes respectively in a single laser resonator; and we further show that when these high-order Gaussian modes are purely in-phase they are reproducible both in the near field and far-field. We demonstrate this by playing a video that shows these frequency-doubled high-order modes in the far-field.

2. Second harmonic generation principle

There are three types of frequency mixing; there is a second harmonic generation (SHG), sum frequency generation (SFG) and difference-frequency generation (DFG). All these three frequency mixing processes involve two pump waves, the fundamental frequencies, ω_1 and ω_2, incident on a nonlinear medium that generates a new wave of frequency ω_3. The generated frequency ω_3, could either be the sum or difference of ω_1 and ω_2, or the second harmonic frequency of each fundamental frequency where both have the same frequency ω_1, and the generated second harmonic beam will have a frequency of $\omega_2 = \omega_1 + \omega_1$. These frequency mixing concepts can be applied to other nonlinear optical interaction but in this article, we will mainly concentrate on the second harmonic generation which is also termed as frequency doubling.

Frequency doubling is generated by the second susceptibility, if one consider a vector field $\mathbf{E} = (E_x, E_y, E_z)$, the second order dielectric polarization $\mathbf{P}^{(2)}$ can be written as follow:

$$M = \begin{bmatrix} P_x^2 \\ P_y^2 \\ P_z^2 \end{bmatrix} = \begin{bmatrix} d_{11} & d_{12} & d_{13} & d_{14} \\ d_{21} & d_{22} & d_{23} & d_{24} \\ d_{31} & d_{32} & d_{33} & d_{34} \end{bmatrix} \begin{bmatrix} E_x^2 \\ E_y^2 \\ E_z^2 \\ 2E_yE_z \\ 2E_xE_z \\ 2E_xE_y \end{bmatrix}, \tag{1}$$

with the dielectric constant of $\epsilon_0 = 8.85 \times 10^{-12} As/(Vm)$, and d_{ij} the nonlinearity coefficients. Furthermore, for loss-free materials, only 10 out of 18 nonlinearity coefficients are independed, also depending on the symmetry of the crystal, the number of the independed coefficients is

considerably reduced so that most frequency doubling crystals will have only two or three independents, and non-zero coefficients remaining. In the case of the KTP, the remaining nonlinearity coefficients are shown in Table 1: If a field $\mathbf{E}^{(1)}$ at the fundamental frequency ω_1 is incident onto the crystal, a field $\mathbf{E}^{(2)}$ at the second harmonic frequency $\omega_2 = 2\omega_1$ is generated at the expense of the fundamental frequency. If we consider the propagation in the z-direction only, the transformation of the field and the electric polarisation into the complex notations is as follows:

$$\mathbf{E}^{(1)} = \frac{1}{2}\left(\mathbf{A}^{(1)}e^{i(\omega_1 t - k_1 z)} + C\right) \tag{2}$$

$$\mathbf{P}^{(1)} = \frac{1}{2}\left(\mathbf{P}_c^{(1)} + \mathbf{P}_c^{*(1)}\right). \tag{3}$$

The electric field $\mathbf{P}$ acts as the source for both fields $\mathbf{E}^{(1)}$ and $\mathbf{E}^{(2)}$, which means that the propagation of each wave is described by the following wave equation:

$$\frac{\delta^2 \mathbf{E}^{(1)}}{\delta z^2} - \frac{1}{c^2}\frac{\delta^2 \mathbf{E}^{(2)}}{\delta t} = -\frac{1}{\epsilon_0}\frac{\delta^2 \mathbf{P}}{\delta t^2}, \tag{4}$$

where c_0 is the speed of light in the medium. The electric field polarization $\mathbf{P}$ is given by the sum of the field $\mathbf{E}^{(1)} + \mathbf{E}^{(2)}$. From Eq. (1), the amplitude $\mathbf{A}$ for the second harmonic and the fundamental is given as follow:

$$2ik_1\frac{\delta A^{(1)}}{\delta z} = \frac{\omega_1^2}{\epsilon_0 c_0^2}P_c^{(2)}(\omega_1)e^{[i(k_1 z - \omega 1 t)]}$$

$$\frac{\delta A^{(1)}}{\delta z} = \frac{2i\omega_1^2}{k_1 c^2}d_{eff}A^{(2)}A^{*(1)}e^{(-i\Delta kz)}, \tag{5}$$

and

$$2ik_2\frac{\delta A^{(2)}}{\delta z} = \frac{\omega_2^2}{\epsilon_0 c_0^2}P_c^{(2)}(\omega_2)e^{[i(k_2 z - \omega_2 t)]}$$

$$\frac{\delta A^{(2)}}{\delta z} = \frac{i\omega_2^2}{k_2 c^2}d_{eff}A^{(1)2}e^{(i\Delta kz)}, \tag{6}$$

Table 1. Non-zero nonlinearity coefficient d_{mn} for KTP.

d_{mn} ($\times 10^{-12}$ m/V)					wavelength λ (nm)
d_{15}	$=$	d_{31}	$=$	$\pm(6.5 \pm 0.5)$	1064
d_{24}	$=$	d_{32}	$=$	$\pm(5.0 \pm 0.5)$	1064
d_{33}	$=$	13.8			1064

where $\mathbf{P}_c^2(\omega)$ represents the components of $\mathbf{P}_c^2$ that oscillates at the frequency ω. The SHG process is then described by the interaction of the two coupled wave equations, Eqs. (5) and (6) inside the nonlinear medium. The amplitude $A^{(2)}$ only increases significantly for $\Delta k = 2k_1 - k_2 = 0$, this is also known as phase-matching. If we consider the frequency doubling as the annihilation of two photons with energy $\hbar\omega_1$ into one photon with energy $\hbar\omega_2$, the phase-matching condition is equivalent to the conservation of momentum:

$$\hbar k_1 + \hbar k_1 = \hbar k_2. \tag{7}$$

Since the wavenumber is related to the frequency and the speed of light using $k = \omega/c$, this relation means that the fundamental wave and the second harmonic must propagate with the

same speed to avoid destructive interference of the second harmonic along with the propagation directions which then avoids dispersion. It is also possible to split the fundamental wave into an extraordinary wave and an ordinary wave to attain phase matching. The parameter phase mismatch, Δk, is then used to assess the degree of these phase analogous phenomena.

When there is a phase mismatch, $\Delta k \neq 0$, this means that different dipoles in the nonlinear crystals oscillate in different phases causing destructive interference within the crystal which will result to a low conversion efficiency of the SHG. This results in the fundamental pump frequency being un-depleted such that the amplitude $A^{(2)} << A^{(1)}$, and the solution of the coupled equations, Eqs. (5) and (6), for a crystal length, L, is given as:

$$A^{(2)}(z = L) = -\frac{i\omega_1}{n_2 c} d_{eff} A^{(1)^2} \frac{Sin(\frac{\Delta kL}{2})}{\frac{\Delta kL}{2}} e^{(\frac{i\Delta kL}{2})}. \tag{8}$$

The above solution clearly shows that the phase mismatch analogous to the coupled equations uses natural birefringence that exists in many nonlinear crystals for either phase-matching or quasi-phase-matching. The term natural birefringence describes the dependency of the refractive index on the direction of polarization of the beam. The angle tuning of the pump beam with respect to the different axes of the nonlinear crystal allows for different polarization combinations to be achieved where there is phase matching.

For nonlinear crystal with refractive index n, the intensities I_1 and I_2 of the fundamental wave and the second harmonic wave are given as follow:

$$
\begin{aligned}
I_2(z) &= I_1(0) tanh^2 \left[\sqrt{\frac{d_{eff}^2 \omega_1^2 I_1(0)}{n^3 2 \epsilon_0 c_0^3}} z \right] \\
&= I_1(0) tanh^2 \left[\frac{z}{L} \right]
\end{aligned} \tag{9}
$$

$$I_1(z) = I_1(0) - I_2(z), \tag{10}$$

where d_{eff} is the effective nonlinear coefficient. The conversion efficiency is defined as the fraction of the fundamental beam power that is converted into the SHG:

$$\eta_{SHG} = tanh^2 \left[\frac{z}{L} \right], \tag{11}$$

where z is the crystal separation and L is the length of the crystal. It is clear from Eq. (11) that at distance $z = L$, 57% of the fundamental beam power can be converted into the second harmonic beam. For a KTP crystal of length 10 mm, the fundamental beam intensity, $I_1(0)$, that will be required to convert 57% of the fundamental power into the SHG, where the fundamental wavelength is 1064 nm, will be 0.026 GW/cm^2. This is significantly less than the KTP crystal damage threshold of 3-3.5 GW/cm^2 [28].

In circular symmetry, the power P_ω of the Gaussian beam with beam radius w and peak intensity I_0 is given by:

$$
\begin{aligned}
P_\omega &= I_0 2\pi \int_0^\infty e^{[-2(r/w)^2]} r dr \quad \text{when} \quad w^2 > 0 \\
&= I_0 \pi \frac{w^2}{2}.
\end{aligned} \tag{12}
$$

It must be noted that increasing the Gaussian mode order and size of the fundamental pump beam will lead to a low conversion efficiency of the SHG beam such that the wings of SHG structure will be less pronounced since the wings of the pump will have less intensity. This will result in

the intensity of the second harmonic field not to be perfectly Gaussian and the SHG power will then be expressed as:

$$P_{2\omega} \quad = \quad I_0 2\pi \int_0^\infty e^{[-2(r/w)^2]} tanh^2[z/Le^{(-r/w)}] r dr. \tag{13}$$

Due to the high-intensity level of the beam inside the laser resonator compared to the beam intensity outside, we opted to place the KTP crystal inside the laser resonator to generate frequency doubled laser beam, as shown in Fig. 1.
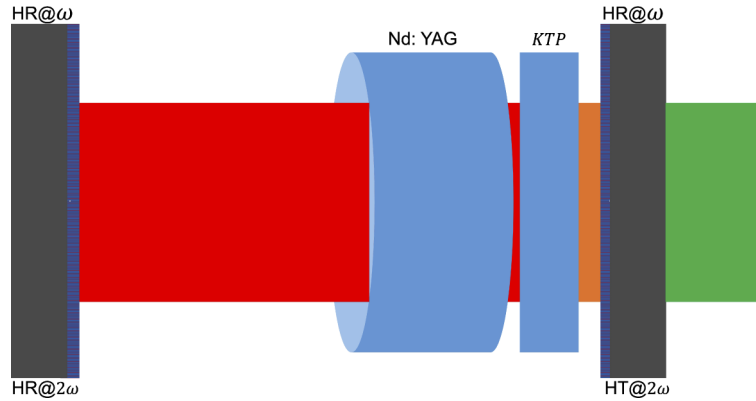

HR@ω

Nd: YAG   KTP

HR@ω

HR@2ω HT@2ω

Fig. 1. Laser resonator model for intracavity frequency doubling from 1064 nm to 532 nm.

As stated before in our introduction, the fundamental beam at 1064 nm is generated by the active medium Nd: YAG and focused on the KTP. From the chosen mirrors in Fig. 1 the conversion efficiency of the KTP acts as the output coupling loss of the laser resonator. If one considers fundamental beam power, P_ω, incident on the KTP crystal and the power of the second harmonic wave generated to be $P_{2\omega}$, then the effect of the KTP crystal on the fundamental beam can be described by the reflectance R as follow:

$$R \quad = \quad 1 - \frac{P_{2\omega}}{P_\omega} \tag{14}$$

$$= \quad 1 - \eta_{SHG}. \tag{15}$$

Thus, the average intensity of I of the fundamental beam inside the Nd: YAG crystal can be calculated using steady-state conditions for round trip [29]:

$$R' = e^{[(2g_0l)/(1+2I/I_s)+2\alpha_0l]}, \tag{16}$$

where I_s is the saturated intensity, g_0l is the small-signal gain and the α_0l is the loss per transit. This steady-state condition is only valid for low signal gain, and high reflectance R because the z-dependence of the fundamental wave intensity inside the KTP is neglected. The second harmonic wave output is given as follow:

$$P_{2\omega} \quad = \quad A_1 I_s \alpha_0 l \left(\sqrt{\frac{g_0l}{\alpha_0l}} - 1 \right), \tag{17}$$

where A_1 is the cross-sectional area of the fundamental beam in the Nd: YAG. One must also keep in mind that although if all the fundamental beam power can be converted into the second harmonic, the conversion efficiency of the KTP crystal may be extremely low. Typically, for diode-pumped Nd: YAG lasers with an efficiency of 48%, the conversion efficiency can be as low as 9.5% [30].

3. Higher-order laser modes

We will be looking at both circular and rectangular symmetry laser modes. The electric field distribution of circular and rectangular laser modes can be written as follow, derived from wave equation:

$$
\begin{aligned}
LG_{p,l}(r,z) = {} & \sqrt{\frac{2p!}{\pi(p+|l|)!}} \times \frac{1}{w(z)} \left(\frac{\sqrt{2}r}{w(z)}\right)^{|l|} \\
& \times L_p^{|l|}\left(\frac{2r^2}{w(z)^2}\right) \times e^{\frac{-r^2}{w(z)^2} - \frac{ikr^2}{2R(z)}} \\
& \times e^{-ikz} \times e^{-il\phi} \times e^{i\psi(p,|l|,z)},
\end{aligned}
\tag{18}
$$

and

$$
\begin{aligned}
HG_{m,n}(r,z) = {} & \sqrt{\frac{1}{2^{m+n} \times m!n!}} \times \frac{1}{w(z)} \times H_n\left(\sqrt{\frac{2x}{w(z)}}\right) \\
& \times H_m\left(\sqrt{\frac{2y}{w(z)}}\right) e^{\frac{-r^2}{w(z)^2} - \frac{ikr^2}{2R(z)}} \\
& \times e^{-ikz} \times e^{i\psi(m,n,z)},
\end{aligned}
\tag{19}
$$

where L_p^l is the Laguerre polynomials [31,32] of order p and l; while H_n and H_m are Hermite polynomials [32,33] of order n and m; and the Lauguerre-Gaussian mode Gouy phase $\psi(p,l,z) = (2p+|l|+1)arctan(\frac{z}{z_0})$ and for Hermite-Gaussian mode the Gouy phase is $\psi(m,n,z) = (|m|+|n|+1)arctan(\frac{z}{z_0})$. All other parameters have their usual meaning as defined in [34]. The lowest-order beam of both Laguerre-Gaussian ($LG_{0,0}$) and Hermite-Gaussian ($HG_{0,0}$) beam has a Gaussian beam profile and is obtained by setting $p = l = 0$ and $n = m = 0$, in Eqs. (18) and (19) respectively. These solutions are often referred to as TEM_{pl} and TEM_{mn} beams, where TEM stands for transverse electric magnetic, within the paraxial approximation, both electric and magnetic fields of the EM wave are, in fact, approximately transverse to the z-direction. The intensity distribution of the TEM_{pl} consists of rings of a central loop for null l indices, and on the other hand for null p indices they take a pattern of petal-like structure. The intensity distribution is given by the absolute square of Eqs. (18) and (19).

For both circular and rectangular symmetries, the propagation and divergence of both LG_{pl} and HG_{mn} modes respectively is shown to be:

$$
w_{pl}(z) = w_0\sqrt{(2p+|l|+1)} \times \sqrt{1+\left(\frac{z}{z_0}\right)^2}, \tag{20}
$$

$$
\theta_{pl} = \theta_0\sqrt{2p+|l|+1} \tag{21}
$$

and

$$
w_m(z) = w_0\sqrt{(2m+1)} \times \sqrt{1+\left(\frac{z}{z_0}\right)^2}, \tag{22}
$$

$$
w_n(z) = w_0\sqrt{(2n+1)} \times \sqrt{1+\left(\frac{z}{z_0}\right)^2}, \tag{23}
$$

$$
w_{m,n}(z) = \frac{w_m(z) + w_n(z)}{2}, \tag{24}
$$

$$
\theta_m = \theta_0\sqrt{2m+1}, \tag{25}
$$

$$\theta_n = \theta_0\sqrt{2n + 1}, \tag{26}$$

where w_0 and θ_0 represents the waist radius and the angle of divergence of the lowest-order fundamental Gaussian beam. The Rayleigh range is defined the same as in Gaussian beam using the following equation:

$$z_0 = \frac{\pi w_0^2}{\lambda}. \tag{27}$$

The beam radius describe by Eqs. (20) and (24) are as a function of the propagation distance from the waist position.

4. Experimental methodology and concept

For the generation of high-order Laguerre-Gaussian ($LG_{p,l}$) and high-order Hermit-Gaussian ($HG_{m,n}$) modes, the planoconcave diode end-pumped solid-state digital laser resonator [35] of length 164 mm, was intracavity inserted with a nonlinear KTP crystal closer to the flat output coupler mirror and a spatial light modulation (SLM) to act as a digital holographic end-mirror of resonator cavity, as shown by the schematic of the experimental setup in Fig. 2. The flat output coupler mirror reflectivity was 90% and the SLM (Hamamatsu LCOS-SLM X10468-03) reflectivity was 95% at a wavelength of 1064 nm respectively. The resonator was designed to form an L-shape in order to avoid illuminating and damaging the SLM with the residual 808 nm pump light by including a 45° mirror (M_1) within the laser resonator cavity that was highly reflective at 1064 nm and highly transmissive at 808 nm. The 1.1% neodymium-doped solid-state gain crystal of 25 mm length and 4 mm diameter was mounted inside a 21 °C water-cooled copper block. The Nd: YAG laser crystal was then end-pumped with a diode laser that could deliver a maximum power of 75 *W* at an operating wavelength of 808 nm and a gain area with a radius of 1.2 mm was excited within the centre of the Nd: YAG rod crystal.
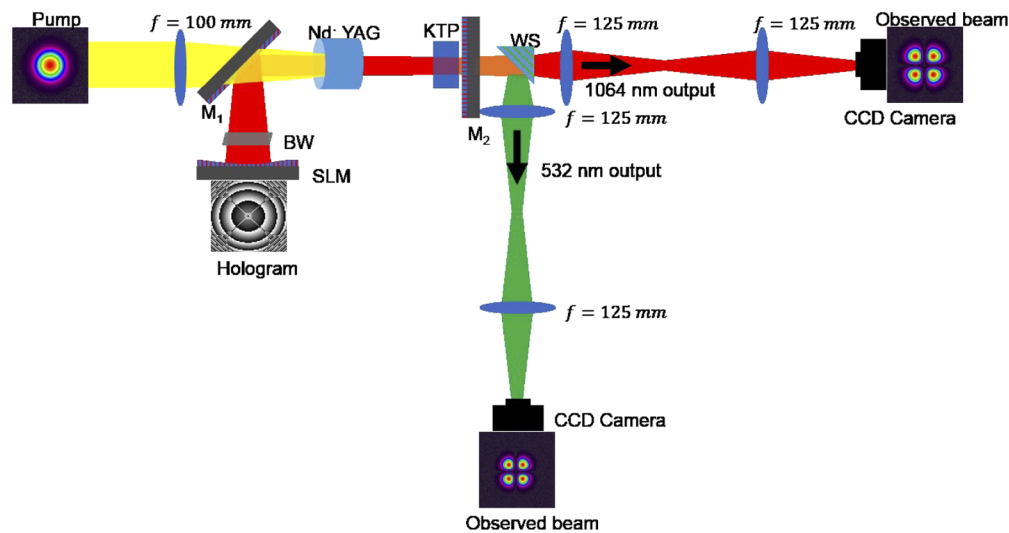

Fig. 2. Schematic of the Nd:YAG crystal digital laser with a non-linear crystal KTP against the output coupler of the resonator.

The SLM was encoded with a reflective grey-scale (0-255) digital holographic image that was displayed on the screen of the SLM inside the laser resonator cavity. The holographic image was encoded to simultaneously control both the phase and amplitude of the fundamental 1064 nm pump mode. The phase of the digital holographic image was used to control the mode size

of the incident fundamental pump mode on to the KTP crystal and the amplitude of the digital holographic image was used to control the type and order of the fundamental pump mode to be either $HG_{m,n}$ or $LG_{p,l}$ respectively. Since the SLM was a phase-only device, yet most of the desired holograms required both the amplitude and phase change to the field, the amplitude effect was encoded on the phase-only SLM using the well-known method of complex amplitude modulation [36,37].

The amplitude of the digital holographic image was encoded to have varying width thickness that were designed to be 98% match each null of the $LG_{p,l}$ or $HG_{m,n}$ mode, for order $p, l = 0, 1, 2$ and $m, n = 0, 1, 2$ as shown in Fig. 3. The SLM was also encoded with digital holograms that had varied the radius of curvature phases, R, from 200 mm to 500 mm with a step size of 50 mm. This was to easily control the mode radius size, w_1, of the fundamental 1064 nm pump mode, and most importantly to also control the angle of acceptance, ψ_j, of the fundamental mode propagating inside the KTP crystal.
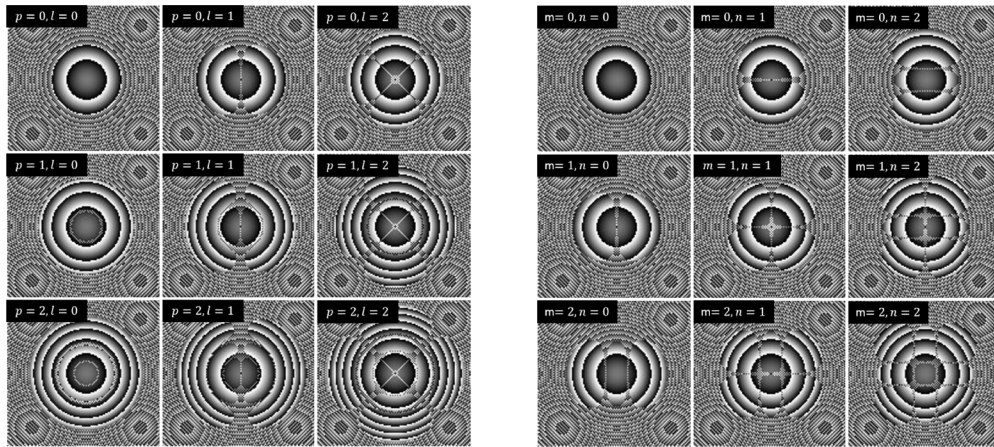

Fig. 3. The grey-scale (0-255) digital holograms that were displayed on the SLM in Fig. 2, for the generation of high-order ($LG_{p,l}$ and $HG_{m,n}$).

The angle tuning of the fundamental 1064 nm pump mode was achieved by varying the radius of curvature of the end-mirror which allowed for various phase-matching conditions of the natural birefringence properties of the nonlinear KTP crystal to be possible for both perfect and quasi-phase-matching. The simulated angle of acceptance, ψ_j, of the fundamental pump mode on to the KTP crystal decreases when the radius of curvature, R, of the holographic end-mirror, is varied from R=200 mm, to R=400 mm, ($\psi_{j,R400} \ll \psi_{j,R200}$), as shown in Fig. 4; When R=400 mm the fundamental pump mode propagating inside the KTP is collinear with almost a constant radius size, w_{1_0}, of 258 μm which allowed for perfect phase matching; And when R=200 mm the fundamental pump mode propagating inside the KTP crystal was at an acute angle which allowed for quasi-phase-matching to occur as the radius size, w_1 of the fundamental pump mode varied inside the crystal from 204 μm to 160 μm. Therefore varying the R of the end-mirror allows for the modulation of the nonlinear coefficients along the X and Y plane of the KTP to take place.

The propagation of the SHG mode with a radius size, w_2, and an amplitude structure, $A^{(2)}$, inside the KTP crystal is designed to be collinear and have a plane wavefront along the entire crystal length, L, as the two faces of the crystal are designed to be flat. Therefore the fundamental pump mode with an amplitude structure, $A^{(1)}$, that has a varying mode radius size, $w_1(z)$, along the KTP crystal length, like in the case of tight focusing using a curved mirror of R=200 mm, will result in the SHG mode not fully matching the phase, the mode structure profile and the radius size of the fundamental pump mode along the entire crystal length from Z_L to Z_0, and
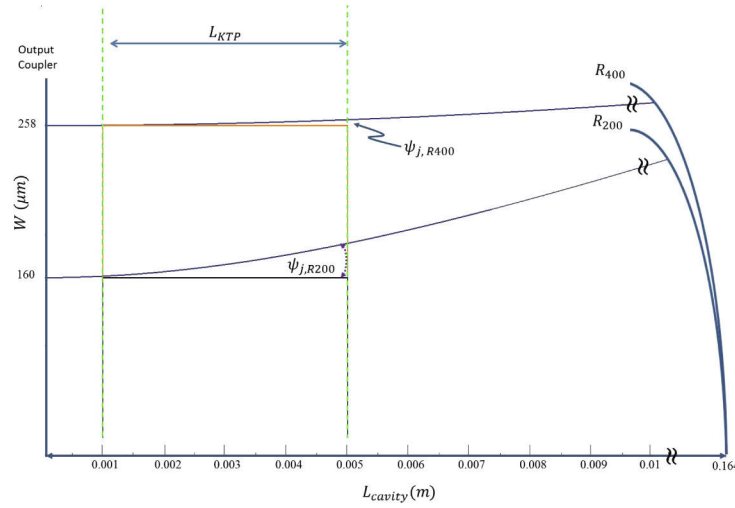
Fig. 4. Schematic of the simulated resonator showing the angle of acceptance, ψ_j, of the fundamental pump mode ($LG_{p=0,l=0}$ or $HG_{m=0,n=0}$) onto the KTP crystal for a 164 mm cavity length with a holographic end-mirror of R=200 mm and R=400 mm. When R=400 mm, the $\psi_{j,4500} \ll \psi_{j,R200}$ which allows for collinear propagation of the fundamental pump mode inside the KTP crystal to occur with a constant mode radius size, w_{1_0}, of 258 μm which allows for perfect collinear phase-matching and conservation of angular momentum to be achieved. When R=200 mm, the fundamental pump mode propagates at an acute angle inside the KTP crystal with varying mode radius size, $w_1(z)$, from 204 μm to 160 μm, which enabled quasi-phase matching to take place.

this will result in the SHG mode not maintaining the mode structure profile of the fundamental pump mode as illustrated in Fig. 5. But at Z_0 to $Z_{L=0}$ of the crystal length, both the fundamental mode amplitude structures, $A^{(1)}$, and the frequency-doubled SHG mode amplitude structure, $A^{(2)}$, are phase-locked and have the same plane wavefront as illustrated in Fig. 5, such that the laser resonator will emit a frequency-doubled SHG mode structure profile, $A^{(2)}$, that will be similar to the fundamental pump mode structure, $A^{(1)}$.

This is because along the propagation direction, Z, the fundamental pump mode acquires a phase shift which differs from that of a plane wave even though the optical frequency is constant and this phase difference is called the Gouy phase shift [27]:

$$\psi(z) = \arctan\left(\frac{z}{z_0}\right) = \arctan\left(\frac{z\lambda}{\pi w_0{}^2}\right). \tag{28}$$

This means that the phase fronts have to propagate somewhat faster leading to an effectively increased local phase velocity. This phase difference is then translated to the created SHG modes such that it results to a slight increased distanced between the wavefronts of modes, $w_{2_{0j}}$, compared with the collinear plane wave mode , w_{2_0}, of the same frequency. The electric field distribution of the SHG modes in circular and rectangular laser modes taking into account the Gouy phase shift can now be represent as:

$$SHG(LG_{p,l}) = \sum_{j=0}^{L} LG_{p,l}(r, z, \psi_j), \tag{29}$$
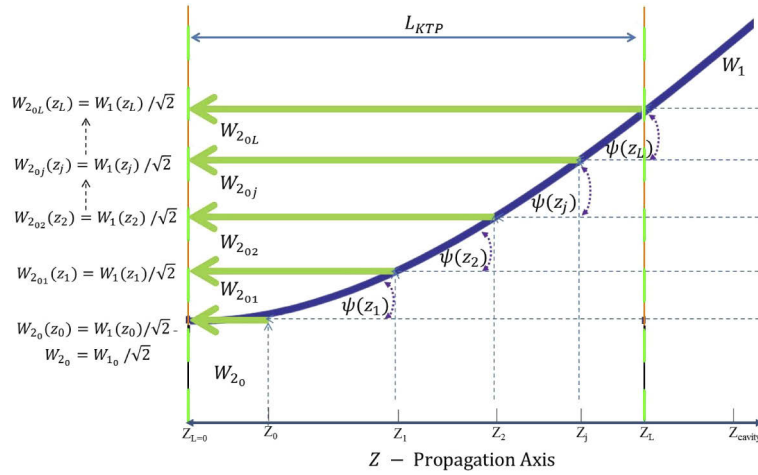
Fig. 5. Schematic of the frequency doubled SHG mode radius, w_{2j}, from the KTP crystal pumped with a varying fundamental mode radius sizes, $w_1(z)$, along the crystal length. The schematic shows that the fundamental pump mode experiences various Gouy phases, $\psi(z_j)$, inside the resonator such that inside the KTP crystals the SHG modes are generated with different mode radius orders sizes, $w_{2_{0j}}$. For $j = 0$, both w_1 and w_2 are collinear and perfect phase matching will occur where the far-field and near-field of the SHG mode amplitude structure of $A^{(2)}$ will be similar to the fundamental amplitude mode structure $A^{(1)}$. For $j \geq 0$ quasi-phase matching of the w_1 and w_2 will occur where near-field of $A^{(2)}$ will be similar to $A^{(1)}$ but not at the far-field. For $j \neq 0$ or $j > 0$, phase matching of the fundamental mode structure will not be achieved even though the laser will generate frequency doubled SHG laser beam.

and

$$SHG(HG_{m,n}) = \sum_{j=0}^{L} HG_{m,n}(r, z, \psi_j), \qquad (30)$$

where

$$\psi_j(z) = \arctan\left(\frac{z\lambda}{\pi w_{2_{oj}}^2}\right), \qquad (31)$$

and

$$w_{2_{oj}} = \frac{w_1(z_j)}{\sqrt{2}}. \qquad (32)$$

The ψ_j represents the different variation in the Gouy phases on the SHG modes with different orders j. It must be understood that the phase shift of a Gaussian beam is not exactly the same as for a plane wave. A Gaussian beam can be considered as a superposition of plane waves with different propagation directions. Those plane wave components with propagation directions different from the beam axis experience smaller phase shifts along the propagation direction, z, and the overall phase shift will arise from a superposition of all these components. For higher-order transverse modes such as $LG_{p,l}$ and $HG_{m,n}$, the Gouy phase shift is stronger by a factor of $2p + l + 1$ and $m + n + 1$ respectively; and this show that the resonance frequencies of higher-order modes in optical resonators will be high. This will then be compensated by adjusting the radius of curvature, R, of the end-mirror such that the propagation wavefront is collinear and plane inside the entire KTP crystal length.

From Eq. (32) it must be understood that when $j = 0$, the fundamental pump mode will be collinear and have a plane wavefront inside the entire crystal length such that the Gouy phase

shift will be constant with $\psi_{j=0}$. This will result in a perfectly phased matched high-order SHG mode that will reproduce the profile structure of the high-order fundamental pump mode. For the generation of quasi-phased high-order SHG modes, $j \geq 0$, and this will result in some of the high-order SHG modes experiencing a phase shift and others not, and those SHG modes that experience a phase shift will produce a mode profile structure that will have a central maximum, that will be surrounded by a phased locked SHG mode. For the generation of non-phased high-order SHG modes, the structure of the fundamental mode will not be reproducible at all on the frequency-doubled SHG mode. The intensity profile of the SHG mode will have mostly a dominant central maximum only, when $j>0$, as all of the SHG modes will experience a Gouy phase shift that will be out-of-phase with the fundamental pump mode, even though the laser will be generating a frequency-doubled SHG laser beam.

The dimensions of the intracavity nonlinear KTP crystal was 3 mm × 3 mm× 3 mm and it was mounted inside a copper block that was not temperature controlled. The nonlinear KTP crystal was highly reflective for 532 nm on the left face diagonal of the crystal where the fundamental 1064 nm pump mode would be the first incident on the KTP crystal, and the right face diagonal of the crystal was highly non-reflective for 532 nm. Both 1064 nm and 532 nm beams exited the output coupler mirror (M_2) parallel to each other. We used a beam splitter that acted as a wavelength separator (WS) to separate the 1064 nm and 532 nm wavelengths beams. Lens f_1 and f_2 were used to relay image the plane of the output coupler mirror for 1064 nm onto the CCD_1, and Lens f_3 and f_4 were used to relay image the plane of the output coupler mirror for 532 nm onto CCD_2 camera, for the characterization of the frequency-doubled SHG laser modes.

5. Results and discussions

The method used to excite high-order modes from the laser cavity was by employing computer-generated hologram masks which were encoded as pixelated grey (0-255) images as shown in Fig. 3 and displayed onto an SLM that also acted as an end mirror of the laser resonator [35]. The results of the observed intensity distribution profiles generated by the laser resonator for Laguerre-Gaussian modes, $LG_{p,l}$, and Hermite-Gaussian modes, $HG_{m,n}$, operating at 1064 nm are shown in Figs. 6(a) and 6(b) respectively, when the radius of curvature of the end-mirror was set at R=200 mm. The 2D-intensity distribution profiles shown in Fig. 6 were captured at the output coupler mirror of the laser resonator. The spatial profile of these fundamental high-order modes remained constant both in the near-field and at the far-field. In addition, we used a ModeScan 1780 to measure M^2 (as shown in Fig. 6(a)), and we found that mode generated were of good quality with only 8% error. This suggests that the generated fundamental laser modes are as shown in [23,35,38]. The experimental results of the mode radius sizes, w_1, of both the fundamental high-order $LG_{p,l}$ and $HG_{m,n}$ modes at the output coupler were compared to the theoretical solution shown in Fig. 7(a) and Fig. 7(b) respectively.

The results in Fig. 7 shows that the mode radius sizes, w_1, of the high-order fundamental ($LG_{p,l}$ and $HG_{m,n}$) modes, ω, that are emitted by the laser resonator cavity were of appropriate dimensions and within the experimental error. At a wavelength of 1064 nm these high-order modes of $LG_{p,l}$ and $HG_{m,n}$ were used as the fundamental pump mode of frequency, ω, to pump the non-linear KTP crystal to produce frequency double, 2ω, second harmonic generated (SHG) high-order modes with similar intensity distribution structure profile. The results of pumping the nonlinear KTP crystal with the fundamental high-order ($LG_{p,l}$ and $HG_{m,n}$) modes, ω, for the SHG of frequency-doubled high-order ($LG_{p,l}$ and $HG_{m,n}$) modes, 2ω, is shown in Fig. 8 below for both the near-field and far-field spatial profiles of the frequency-doubled modes, respectively, when the radius of curvature of the end-mirror was set at R=200 mm.
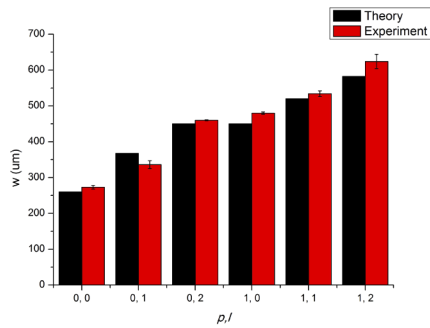
The near-field spatial intensity profiles of the SHG $LG_{p,l}$ modes, 2ω, in Fig. 8(a) is similar to the intensity profile of the fundamental $LG_{p,l}$ pump modes, ω shown in Fig. 6(a); But at the far-field the spatial intensity profiles of the SHG $LG_{p,l}$ modes, 2ω, as shown in Fig. 8(b), is different from
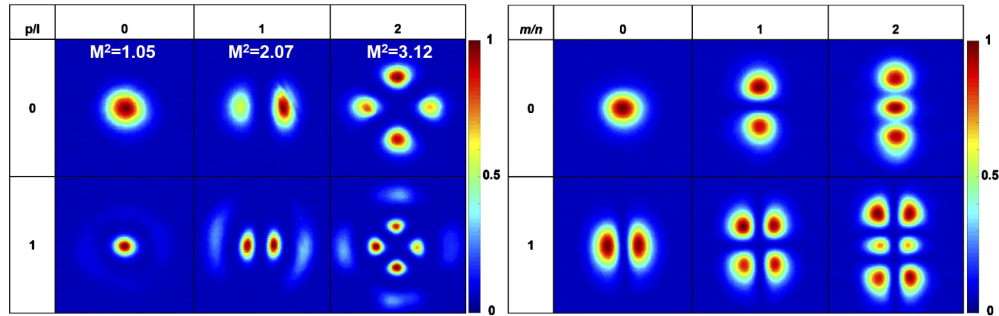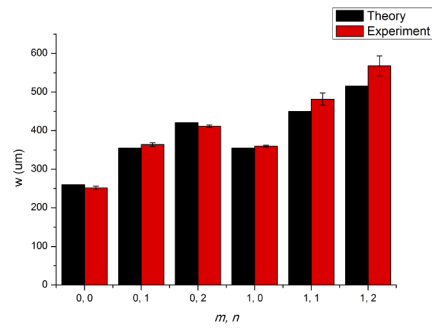
(a) Fundamental $LG_{p,l}$ mode profiles, ω.

(b) Fundamental $HG_{m,n}$ mode profiles, ω.

Fig. 6. The observed intensity profiles for the fundamental pump modes, ω, of $LG_{p,l}$ (for $p = 0, 1$ & $l = 0, 1, 2$) and $HG_{m,n}$ (for $m = 0, 1$ & $n = 0, 1, 2$) high-order modes when the radius of curvature of the end-mirror was set at R=200 mm.
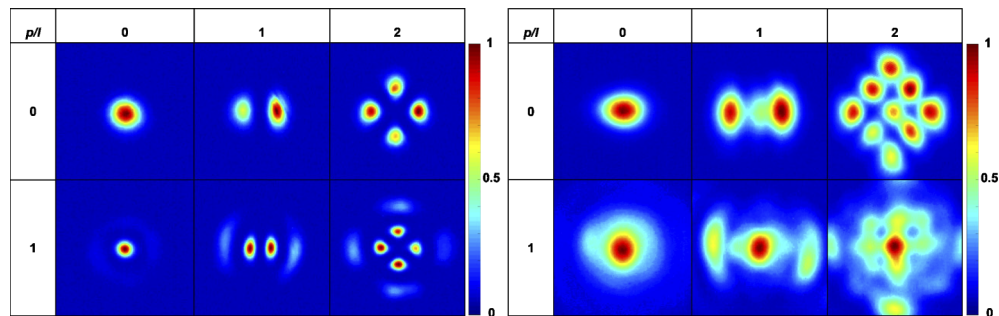

(a) Fundamental, ω, $LG_{p,l}$ mode radius, w_1.

(b) Fundamental, ω, $HG_{m,n}$ mode radius, w_1.

Fig. 7. Shows the fundamental mode, ω, radius sizes, w_1, as the function of mode-order ($LG_{p,l}$ and $HG_{m,n}$) at the output coupler when the radius of curvature of the end-mirror is set at R=200 mm.

(a) SHG $LG_{p,l}$ modes, 2ω, at near-field.

(b) SHG $LG_{p,l}$ modes, 2ω, at far-field.

Fig. 8. The observed intensity profiles, 2ω of the SHG $LG_{p,l}$ modes at the near-field, (a), and at the far-field, (b), respectively. At the near-field the SHG $LG_{p,l}$ modes, 2ω, is phase-matched with the fundamental $LG_{p,l}$ pump modes, ω; While at the far-field the SHG $LG_{p,l}$ modes, 2ω, is quasi-phased with the fundamental $LG_{p,l}$ pump modes, ω, as there is a dominant central maximum.

the fundamental LG$_{p,l}$ pump mode, ω, as there is an added central intensity maximum for LG$_{0,2}$, LG$_{1,0}$, LG$_{1,1}$ and LG$_{1,2}$. The SHG of LG$_{0,1}$ mode shows a slight deformation of the intensity distribution structure profile at FF which also confirms that there was a quasi-phase-matching of the fundamental pump mode. This phenomena also occurs for the SHG of HG$_{m,n}$ modes, 2ω, as shown in Fig. 9, where the near-field spatial profiles of the SHG HG$_{m,n}$ modes, 2ω, is similar to the fundamental HG$_{m,n}$ pump modes; But at the far-field the SHG HG$_{m,n}$ modes also have an added central intensity maximum for the HG$_{0,2}$ and HG$_{0,3}$ modes. The SHG of the HG$_{0,1}$ showed that this mode was similar at near-field and far-field and also to the fundamental pump mode.
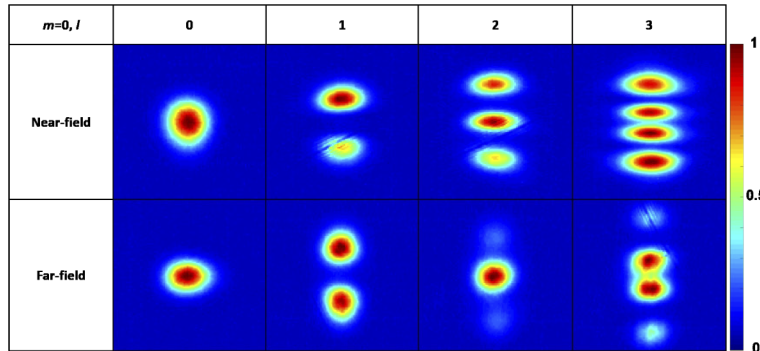

Fig. 9. The observed intensity profile, 2ω, of the SHG HG$_{m,n}$ modes at the near-field and at the far-field, respectively. At the near-field the SHG HG$_{m,n}$ mode, 2ω, is phase-matched with the fundamental HG$_{m,n}$ pump modes, ω; While at the far-field the SHG HG$_{m,n}$ mode, 2ω, is quasi-phased with the fundamental HG$_{m,n}$ pump mode, ω.

The non-reproducibility of the far-field spatial intensity profiles of the SHG LG$_{p,l}$ and SHG HG$_{m,n}$ modes when compared to the near-field spatial intensity profiles, which is similar to the fundamental pump mode, is due to quasi-phase-matching of the modes inside the KTP crystal. The SHG high-order modes experience various Gouy phases, where some of the phases of the SHG modes are partly in-phase and others out-phase with the fundamental pump mode.

The generation of high-order quasi-phased SHG modes at far-field shows that fundamental pump mode was not propagating perfectly collinearly inside the entire length of the nonlinear KTP crystal. This resulted in some of the SHG modes to be in-phase at the near-field and some to be out-of-phase with the fundamental pump mode. To achieve perfect phase-matching, the radius of curvature, R, of the end-mirror was increased in steps of 50 mm by simply displaying rewritable digital holograms of appropriate R on the SLM without any realignment of the laser resonator. This incremental adjustment allowed for the evaluation of the correct radius of curvature to be selected where the fundamental pump mode will have a constant mode radius, w_{1_0}, and a collinear spatial profile of the mode that will have a plane wavefront along the entire length of the KTP crystal.

We discovered that when the end-mirror is set at R=400 mm which equated to a fundamental Gaussian (LG$_{00}$ or HG$_{00}$) mode radius size of w_0=258 μm. The SHG high-order modes both at the far-field and near-field, their intensity structure profiles were similar to the fundamental pump mode profiles. This demonstrated that at R=400 mm the fundamental modes were perfectly in-phase with the SHG modes and these results are shown in Fig. 10 for generation of both the SHG HG$_{m,n}$ and SHG LG$_{p,l}$ modes. It is clear in Fig. 10 that the intensity structure profiles of the SHG high-order modes are similar at the far-field and at the near-field for all the LG$_{p,l}$ and HG$_{m,n}$ modes. We performed additional analysis of the emitted SHG LG$_{p,l}$ and HG$_{m,n}$ modes radius sizes by comparing them to the theoretical values using Eqs. (20) and (22), where the estimated fundamental Gaussian mode radius size, w_0, of the resonator with an end-mirror of

R=400 mm is 258 μm [39], which is then divided by $\sqrt{2}$ so as to phase-match the SHG modes as shown by Eq. (32) since all these modes are generated by a stable resonator. Furthermore, we used a ModeScan 1780 to measure M^2 for SHG $LG_{p,l}$ (as shown in Fig. 10(b)), and we found that mode generated were of reasonable quality with 11% error.
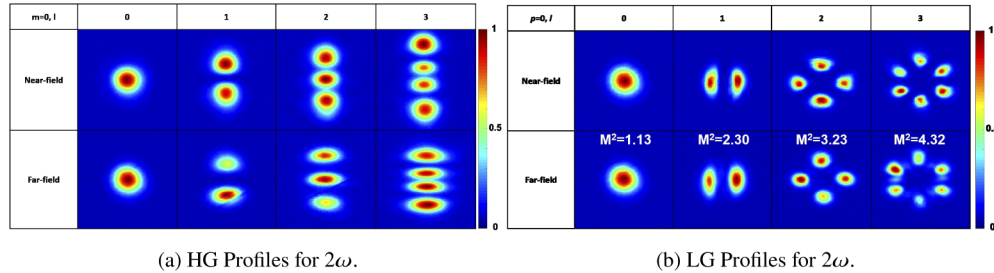

(a) HG Profiles for 2ω.

(b) LG Profiles for 2ω.

Fig. 10. The observed intensity profiles, 2ω, of SHG high-order modes for (a) $HG_{m,n}$ and $LG_{p,l}$ modes at the near-field and far-field for in-phase fundamental pump modes, ω.

The experimental results of the SHG $LG_{p,l}$ and $HG_{m,n}$ mode radius sizes, w_2 in Fig. 11 clear shows that the resonator was emitting the correct SHG high-order modes when compared to the theoretical values. The experimental mode radius sizes of SHG $LG_{p,l}$ were in very good agreement with the theoretical values as most of the values were within the error margin. There was also a general undervaluing of the $HG_{m,n}$ mode radius of $HG_{0,2}$, $HG_{1,0}$, $HG_{1,1}$ and $HG_{1,2}$. All of these experimental deviations were due to misalignment of the laser resonator which produced asymmetrical radius mode values for $HG_{m,n}$ modes and this is shown by the $HG_{0,1}$ and $HG_{1,0}$ mode radii which were supposed to be of similar values as the two modes are reciprocal and orthogonal in shape to another. The misalignment of the laser resonator caused the radius size of the $HG_{0,1}$ mode to increase by an equivalent value at which the $HG_{1,0}$ radius mode decreased, such that taking the average of the two theoretical values results to matching the predicted theoretical value of the two modes.
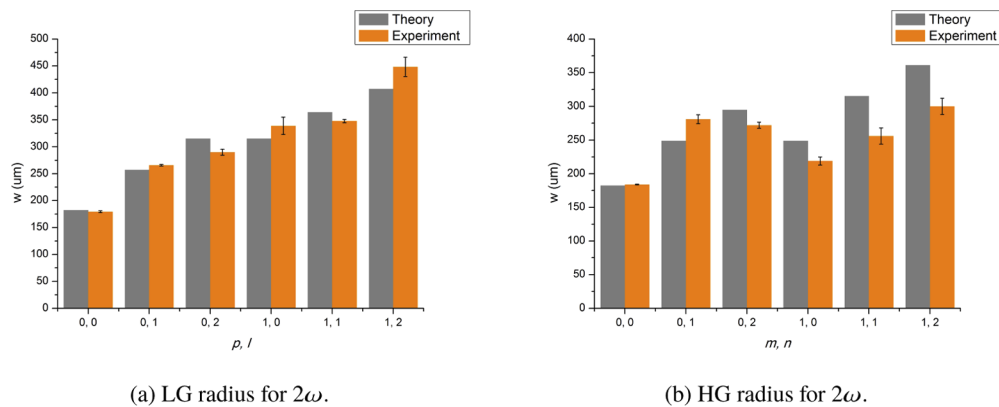

(a) LG radius for 2ω.

(b) HG radius for 2ω.

Fig. 11. The SHG, 2ω, for (a) $HG_{p,l}$ and (b) $LG_{p,l}$ mode radius sizes, w_2, as the function of mode order at the output coupler when the radius of curvature of the end-mirror is set at R=400 mm.

In addition, the laser resonator slope efficiency of the fundamental mode, ω, of $LG_{0,0}$, and $LG_{0,3}$ are shown in Fig. 12(a). The slope efficiency for the $LG_{0,0}$ is 4%, while for the $LG_{0,3}$ is 8%. The higher-order mode of $LG_{0,3}$ has a high slope efficiency and laser threshold since it's mode volume is larger than $LG_{0,0}$ and this is in very good agreement with previous results in [23,24].

The slope efficiency for the SHG modes, 2ω, of $LG_{0,0}$ is 0.2% and of $LG_{0,3}$ is 0.1% as shown in Fig. 12(b). The slope efficiency of the 2ω, $LG_{0,0}$ is higher compared to the $LG_{0,3}$ because the SHG process is an intensity driven process and the 2ω, $LG_{0,0}$ modes has more power per unit area compared to $LG_{0,3}$. The results show that the output power of the SHG modes to be on the mill-watt range and the slope efficiency lines to be not very straight. This is because the KTP crystal was not temperature controlled but was mounted on a copper heat sink and air-cooled. The overall results demonstrate that the laser resonator was producing phase-matched SHG $LG_{p,l}$ and $HG_{m,n}$ modes that are in good agreement with theory and also that maintain their intensity mode structure both at the near-field and far-field.
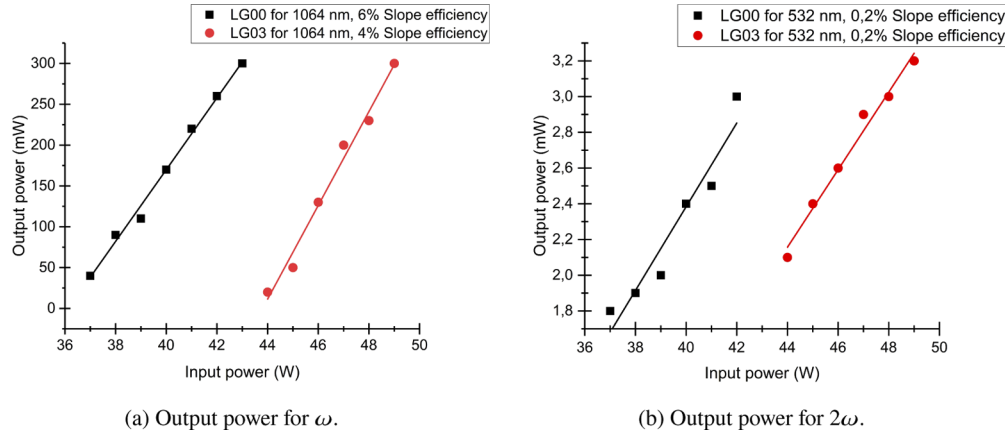

(a) Output power for ω.

(b) Output power for 2ω.

Fig. 12. The output power in watts as the function of absorbed power in milliwatts for $LG_{p,l}$.

6. Conclusion remarks

We have successfully converted high-order Laguerre-Gaussian and Hermite-Gaussian modes operating at 1064 nm to high-order Laguerre-Gaussian and Hermite-Gaussian modes operating at 532 nm. The intensity profile distributions of the SHG beams at the far-field and the near-field were comparable with a high degree, the M^2 of the LG beams were measured and they are in good agreement with theory. The next step in our research is to increase the slope efficiency of both the 1064 nm and the 532 nm laser beams and measure the purity of the beams.

Funding

Acknowledgments

Disclosures

The authors declare no conflicts of interest.

References

1. E. Y. Chan, N. M. Goncalves, R. A. Haeusler, A. J. Hatch, and J. W. Larson, "Dna mapping using microfluidic stretching and single-molecule detection of fluorescent site-specific tags," Genome Res. **14**(6), 1137–1146 (2004).
2. J. L. Hall, J. Ye, S. A. Diddams, L.-S. Ma, S. T. Cundiff, and D. J. Jones, "Ultrasensitive spectroscopy, the ultrastable lasers, the ultrafast lasers, and the seriously nonlinear fiber: a new alliance for physics and metrology," IEEE J. Quantum Electron. **37**(12), 1482–1492 (2001).
3. J. J. Degnan, "Satellite laser ranging: current status and future prospects," IEEE Transactions on Geosci. Remote. Sens. **GE-23**(4), 398–413 (1985).
4. G. G. L. S. Duo-Min He, "Laser gated-ranging for underwater robot vision in turbid waters," (2002), pp. 11–23.
5. F. Bandello, R. Brancato, R. Lattanzio, G. Trabucchi, C. Azzolini, and A. Malegori, "Double-frequency nd: Yag laser vs. argon-green laser in the treatment of proliferative diabetic retinopathy: Randomized study with long-term follow-up," Lasers Surg. Med. **19**(2), 173–176 (1996).
6. Y. Zheng, H. Liu, Y. Wang, C. Zhu, S. Wang, J. Cao, and S. Zhu, "Accumulating microparticles and direct-writing micropatterns using a continuous-wave laser-induced vapor bubble," Lab Chip **11**(22), 3816–3820 (2011).
7. J. Yin, J.-G. Ren, H. Lu, and Y. Cao, "Quantum teleportation and entanglement distribution over 100-kilometre free-space channels," Nature **488**(7410), 185–188 (2012).
8. T. Wiener and S. Karp, "The role of blue/green laser systems in strategic submarine communications," IEEE Trans. Commun. **28**(9), 1602–1607 (1980).
9. Y. Lin, K. Huang, and Y. Chen, "The formation of quasi-nondiffracting focused beams with second-harmonic generation of flower laguerre–gaussian modes," Laser Phys. **23**(11), 115405 (2013).
10. L. Bell and S. Ngcobo, "Intracavity second harmonic generation for higher-order laser modes," in *Laser Resonators, Microresonators, and Beam Control XXI*, vol. 10904 (International Society for Optics and Photonics, 2019), p. 109041P.
11. A. Shapira, L. Naor, and A. Arie, "Nonlinear optical holograms for spatial and spectral shaping of light waves," Sci. Bull. **60**(16), 1403–1415 (2015).
12. X. Li, X. Shen, and G. Li, "Cyclic variation of output energy with ambient temperature changes in intracavity ktp frequency-doubling laser," Optik (Munich, Ger.) **126**(2), 279–282 (2015).
13. S. F. Liew, S. Knitter, S. Weiler, J. F. Monjardin-Lopez, M. Ramme, B. Redding, M. A. Choma, and H. Cao, "Intracavity frequency-doubled degenerate laser," Opt. Lett. **42**(3), 411–414 (2017).
14. M. E. Hagerman and K. R. Poeppelmeier, "Review of the structure and processing-defect-property relationships of potassium titanyl phosphate: a strategy for novel thin-film photonic devices," Chem. Mater. **7**(4), 602–621 (1995).
15. Z. Kecong and W. Ximin, "Structure sensitive properties of ktp-type crystals," Chin. Sci. Bull. **46**(24), 2028–2036 (2001).
16. D. N. Nikogosyan, *Nonlinear optical crystals: a complete survey* (Springer Science & Business Media, 2006).
17. V. G. Dmitriev, G. G. Gurzadyan, and D. N. Nikogosyan, *Handbook of nonlinear optical crystals*, vol. 64 (Springer, 2013).
18. C. Defan and Y. Zhengtang, "Investigation on some properties of ktiopo 4 crystals," J. Cryst. Growth **79**(1-3), 974–977 (1986).
19. R. Ganeev, I. Kulagin, A. Ryasnyansky, R. Tugushev, and T. Usmanov, "Characterization of nonlinear optical parameters of kdp, linbo 3 and bbo crystals," Opt. Commun. **229**(1-6), 403–412 (2004).
20. R. Weis and T. Gaylord, "Lithium niobate: summary of physical properties and crystal structure," Appl. Phys. A **37**(4), 191–203 (1985).
21. T. Bell, S. Ngcobo, and A. Forbes, "Generation of laguerre-gaussian beams using a Solid State Digital laser," in *Frontiers in Optics*, (Optical Society of America, 2015), pp. FW6B–3.
22. T. Bell, A. Hasnaoui, K. Äit-Ameur, A. Forbes, and S. Ngcobo, "Intracavity generation of low-loss radial-order Laguerre-Gaussian modes using digital holograms," in *SPIE LASE*, vol. 9727 (International Society for Optics and Photonics, 2016), p. 97271K.
23. T. Bell and S. Ngcobo, "Selective excitation of higher-radial-order laguerre-gaussian beams using a solid-state digital laser," J Laser Opt Photonics **3**(2), 144 (2016).
24. T. Bell, A. Hasnaoui, K. Ait-Ameur, and S. Ngcobo, "Excitation of high-radial-order laguerre–gaussian modes in a solid-state laser using a lower-loss digitally controlled amplitude mask," J. Opt. **19**(10), 105604 (2017).
25. T. Bell and S. Ngcobo, "Extra-cavity amplification of the digital laser modes using nd: Yag amplifier," in *CLEO: QELS_Fundamental Science*, (Optical Society of America, 2018), pp. JTu2A–177.
26. Z.-Y. Zhou, D.-S. Ding, Y.-K. Jiang, Y. Li, S. Shi, X.-S. Wang, and B.-S. Shi, "Orbital angular momentum light frequency conversion and interference with quasi-phase matching crystals," Opt. Express **22**(17), 20298–20310 (2014).
27. J. Courtial, K. Dholakia, L. Allen, and M. Padgett, "Second-harmonic generation and the conservation of orbital angular momentum with high-order laguerre-gaussian modes," Phys. Rev. A **56**(5), 4193–4196 (1997).
28. F. Ahmed, "Laser damage threshold of ktiopo$_4$," Appl. Opt. **28**(1), 119–122 (1989).
29. R. G. Brewer and E. Hahn, "Coherent two-photon processes: Transient and steady-state cases," Phys. Rev. A **11**(5), 1641–1649 (1975).

30. W. J. Kozlovsky, C. Nabors, and R. L. Byer, "Efficient second harmonic generation of a diode-laser-pumped cw nd: yag laser using monolithic mgo: linbo/sub 3/external resonant cavities," IEEE J. Quantum Electron. **24**(6), 913–919 (1988).

31. H. E. Salzer and R. Zucker, "Table of the zeros and weight factors of the first fifteen laguerre polynomials," Bull. Amer. Math. Soc. **55**(10), 1004–1013 (1949).

32. M. Abramowitz and I. A. Stegun, *Handbook of mathematical functions* (Applied mathematics series, 1966).

33. H. E. Salzer, R. Zucker, and R. Capuano, *Table of the zeros and weight factors of the first twenty Hermite polynomials* (US Government Printing Office, 1952).

34. B. A. Lengyel, *Introduction to laser physics* (John Wiley And Sons, 1966).

35. S. Ngcobo, I. Litvin, L. Burger, and A. Forbes, "A digital laser for on-demand laser modes," Nat. Commun. **4**(1), 2289 (2013).

36. V. Arrizón, "Optimum on-axis computer-generated hologram encoded into low-resolution phase-modul ation devices," Opt. Lett. **28**(24), 2521–2523 (2003).

37. V. Arrizón, U. Ruiz, R. Carrada, and L. A. González, "Pixelated phase computer holograms for the accurate encoding of scalar complex fields," J. Opt. Soc. Am. A **24**(11), 3500–3507 (2007).

38. D. Naidoo, K. Aït-Ameur, M. Brunel, and A. Forbes, "Intra-cavity generation of superpositions of laguerre–gaussian beams," Appl. Phys. B **106**(3), 683–690 (2012).

39. L. Bergstein, "Modes of stable and unstable optical resonators," Appl. Opt. **7**(3), 495–504 (1968).